



The interplay of sulfur doping and surface hydroxyl in band gap engineering: Mesoporous sulfur-doped TiO₂ coupled with magnetite as a recyclable, efficient, visible light active photocatalyst for water purification

Xiaoqing Yan^a, Kun Yuan^a, Nan Lu^a, Hanjiao Xu^a, Siyu Zhang^a, Nobuyuki Takeuchi^b, Hisayoshi Kobayashi^b, Renhong Li^{c,*}

^a Department of Chemistry, Zhejiang Sci-Tech University, Hangzhou, 310018, China

^b Department of Chemistry and Materials Technology, Kyoto Institute of Technology, Matsugasaki, Sakyo-ku, Kyoto 606-8585, Japan

^c Department of Materials Engineering, College of Materials and Textiles, Zhejiang Sci-Tech University, Hangzhou, 310018, China

ARTICLE INFO

Article history:

Received 24 March 2017

Received in revised form 26 May 2017

Accepted 8 June 2017

Available online 9 June 2017

Keywords:

TiO₂

Visible light

Sulfur doping

Surface hydroxyl

Magnetite

ABSTRACT

Photocatalysis based on TiO₂ offers a sustainable pathway to drive chemical reactions, such as water splitting and contaminants decomposition, while band gap engineering of TiO₂ is necessary to achieve a visible light response. Herein, we prepare sulfur doped TiO₂ (TiO₂-S) photocatalyst by using titanium sulfate as a dual precursor for both of TiO₂ and S in a one-pot synthetic strategy. Meanwhile, pre-synthesized Fe₃O₄ nanoparticles are coupled onto TiO₂-S via a hydrothermal method. The resulting Fe₃O₄/TiO₂-S composites with plenty of surface hydroxyl groups act as an efficient photocatalyst for decomposition of Rhodamine B and formaldehyde solution under visible light and solar light irradiation. On the basis of density functional theory (DFT) calculations and experimental observations, we suggest that the electronic interaction induced synergetic effect of doped sulfur and surface hydroxides can not only significantly narrow the band gap (individual surface hydroxyls or S-doping has no such a great effect), but also enhances the surface hydrophilicity of TiO₂, ultimately making itself a robust visible light photocatalyst for organic pollutants decomposition. Thus, this dual nonmetal modification strategy is proved to exert an enormous function on band gap engineering of semiconductor photocatalyst. In addition, Fe₃O₄/TiO₂-S photocatalyst is superparamagnetic and possesses excellent magnetic responsivity and redispersibility, which is advantageous to their photocatalytic applications.

© 2017 Elsevier B.V. All rights reserved.

1. Introduction

Water pollution is a major global problem, which is considered to be the leading worldwide cause of deaths and diseases [1,2]. To remove organic contaminants in wastewater, one of the “green” and sustainable technologies is heterogeneous photocatalysis driven by solar energy [3–11]. The merits of using environmentally friendly oxidant O₂, ambient reaction conditions, and complete oxidation of the organics compounds to CO₂ and H₂O make photocatalysis outperforming other treatment alternatives. To date, TiO₂ has been undoubtedly demonstrated to be an excellent photocatalyst for the oxidative decomposition of many organic

compounds under UV irradiation, while unfortunately its wide band gap (3.2 eV for anatase phase and 3.0 eV for rutile phase) limits its further application in the visible region ($\lambda > 400$ nm) [12–19]. As the largest proportion of the solar spectrum and artificial light sources, visible light should be effectively utilized, thus the development of a photocatalyst with high visible light activity is of great importance. Typically, cationic doping with transition metal ions is commonly used to tailor the bandgap energies of photocatalysts [20–24]. In this case, the response to visible light is mainly due to high levels of impurities in the forbidden energy band of the photocatalysts, which could serve as recombination centers for photoinduced charges and thus reduce the photocatalytic activity. Previous studies have also shown that modification of TiO₂ by doping with nonmetals, such as nitrogen [25–27], carbon [28–31], phosphor [32–34], and boron [35,36] could extend its light absorption edge from UV to visible light region and consequently

* Corresponding author.

E-mail address: lirenhong@zstu.edu.cn (R. Li).

introduce substantial visible light photocatalytic activity. Among these dopants, sulfur (S) doping is one of the most effective strategies, due to its high thermal stability and significant enhancement in visible light driven photocatalytic activity [37–49]. To successfully incorporate S atoms into the TiO_2 crystals, TiS_2 , CS_2 , thiourea, etc., are usually employed as the S sources, while they are either toxic or expensive. To our knowledge, so far there are limited reports on the fabrication of visible light responsive mesoporous S-doped TiO_2 (denoted as TiO_2 -S hereafter) photocatalyst by using titanium sulfate ($\text{TiOSO}_4 \cdot x\text{H}_2\text{SO}_4 \cdot 8\text{H}_2\text{O}$) as a dual precursor for both of TiO_2 and S in a one-pot synthetic strategy.

In addition, a photocatalyst slurry reactor is one of the most commonly applied systems to deal with pollutants in water due to its higher efficiency as compared with the immobilized counterparts. However, as nanoparticulate powders, TiO_2 slurry will result in the secondary pollution of water unless they can be recycled after photocatalysis. Therefore, magnetically separable TiO_2 -based photocatalyst by coupling with magnetite is indispensable to avoid this problem [19,50]. Herein, we individually prepare TiO_2 -S photocatalyst and superparamagnetic Fe_3O_4 magnetite nanoparticles, and subsequently combine them by hydrothermal treatment to ultimately fabricate recyclable mesoporous $\text{Fe}_3\text{O}_4/\text{TiO}_2$ -S heterostructures. More importantly, the hydrothermal treatment introduces a mass of hydroxyl groups on the photocatalyst surface, which pushes forward an immense influence on the photocatalytic activity of $\text{Fe}_3\text{O}_4/\text{TiO}_2$ -S. Based on DFT calculations and experimental observations, an electronic interaction induced synergetic effect between S-doping and surface hydroxyls is determined, which decreases the band gap of TiO_2 on a large scale. Meanwhile, the reduced band gap and the newly formed impurity energy levels enable the production of hydroxyl radicals as the primary oxidant during visible light photocatalytic reaction. Consequently, the interplay of S-doping and surface hydroxyl groups finally makes mesoporous $\text{Fe}_3\text{O}_4/\text{TiO}_2$ -S an efficient visible light active photocatalysts for decomposition of organic pollutants. Therefore, for the first time, the synchronous modification of surface and bulk state by a dual nonmetal modification strategy is demonstrated to be a new route to the successful band gap engineering of a semiconductor.

2. Experimental

2.1. Photocatalysts synthesis

2.1.1. S-doped mesoporous TiO_2 (TiO_2 -S)

In a typical synthesis, 0.0625 mol of $\text{TiOSO}_4 \cdot 0.13\text{H}_2\text{SO}_4 \cdot 1.5\text{H}_2\text{O}$ was dissolved in 100 mL deionized water, and was continuously stirred at 60 °C for 30 min (denoted as solution A). Certain amount of surfactants CTAB and template P123 were dissolved in the composite solution of ethanol and water ($V_{\text{ethanol}}:V_{\text{H}_2\text{O}} = 1:3$) under vigorous stirring for 1 h (Solution B). Solution A was added into solution B dropwise under stirring, and the pH value of the reaction system was controlled at about 1.0 by adding ammonia (1:1, Vol.%). The molar ratio of $\text{Ti}/\text{CTAB}/\text{P123}$ was 1:0.1:0.01, and the total molar ratio of $\text{H}_2\text{O}/\text{Ti}$ was 140:1. After another 2 h stirring and 3 h static at ambient temperature, the solution with milk-white colloid deposit occurred. Then the solution was transferred into a 500 mL beaker, sealing and aging for 12 h. The resulting gel was filtered, washed repeatedly with distilled water and dried in an oven at 60 °C overnight. Finally, the as-synthesized samples were calcined in air using a heating rate of 2 °C/min, and maintained at 550 °C for 3 h to remove the template.

2.1.2. Fe_3O_4 nanoparticles

Water-dispersible magnetite nanoparticles were synthesized using one-step reverse precipitation method in the presence of

sodium citrate [51]. The magnetite nanoparticle formation is based on aging $\text{Fe}(\text{OH})_2$ gels at 90 °C for 5 h in the presence of KNO_3 as an oxidizing agent. Typically, 0.83 mL 0.50 M KNO_3 was firstly added to 100 mL 0.10 M KOH solution, the obtained transparent solution was degassed with nitrogen for 30 min; then 200 mL of 25 mM $\text{FeSO}_4 \cdot 7\text{H}_2\text{O}$ and a pre-determinate amount of sodium citrate solution was added to this solution under stirring of 600 rpm. After being stirred for 1 h, the resultant black solution was heated to 90 °C and maintained at this temperature for 5 h. The reaction was protected under nitrogen to void the uncontrollable oxidizing effect of air. After being cooled down to room temperature, the as-prepared magnetite nanoparticles were precipitated by acetone to move the excessive sodium citrate, and then the as-prepared magnetite nanoparticles were collected with a permanent magnet and vacuum dried at 30 °C over night.

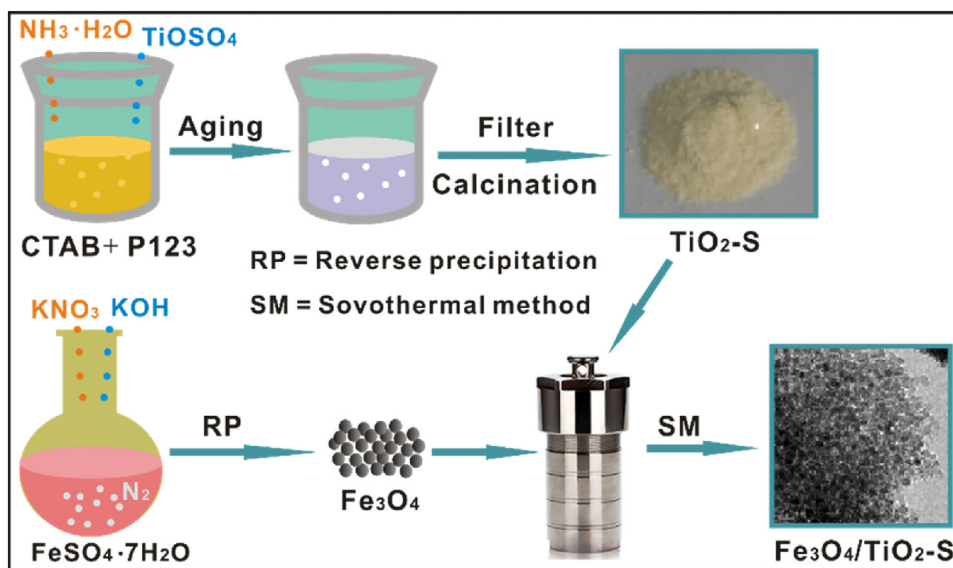
2.1.3. $\text{Fe}_3\text{O}_4/\text{TiO}_2$ -S

15 or 30 mg Fe_3O_4 as-synthesized nanoparticles and 60 mL acetone were added into a single neck flask, and then sonicated for 30 min 300 mg TiO_2 powders were added and stirred for 2 h. After the upper solution becoming transparent, the precipitate was collected by a magnet, which was then transferred into a 100 mL hydrothermal reactor with a certain amount of glycol. The hydrothermal reaction was maintained at 180 °C for 24 h before it is cooled to room temperature. The precipitate was collected by magnet and washed by ethanol for 3 times, and finally dried at 60 °C in vacuum over night. The final powder was $\text{Fe}_3\text{O}_4/\text{TiO}_2$ -S photocatalyst and kept under Ar protection before use.

2.2. Characterizations

High-resolution X-ray photoelectron spectroscopy (XPS) measurements were performed in a VG Scientific ESCALAB Mark II spectrometer equipped with two ultrahigh vacuum (UHV) chambers. All binding energies were referenced to the $\text{C}1s$ peak at 284.6 eV of the surface adventitious carbon. Wide-angle XRD patterns were recorded on a Bruker D8 diffractometer using $\text{CuK}\alpha$ radiation. Nitrogen adsorption-desorption analysis was carried out at 77 K on a Micromeritics ASAP 2020 adsorption analyzer. Before the adsorption analysis, calcined samples were outgassed under a vacuum at 200 °C in the port of the adsorption analyzer. Transmission electron microscopy (TEM) images were taken using a JEOL 2010 electron microscope operating at 80 keV. X-band EPR signals were recorded at ambient temperature on a Bruker EPR A-300 spectrometer. The settings for the EPR spectrometer were as follows: center field, 3511.39 G; sweep width, 100 G; microwave frequency, 9.86 G; modulation frequency, 100 kHz; power, 101 mW; conversion time, 10 mS. The spin trapping experiments were performed as follows: The solid catalyst (~5.0 mg) was mixed with calculated amount of ice-cooled DMPO solution (0.08 M) in the presence of aqueous methanol solution (0.1 M). The mixture was quickly transferred into a glass capillary tube and tested by EPR spectroscopy at room temperature with visible light irradiation. A 100 W Hg lamp (LOT Oriel) with an optical filter was used to provide visible light with $\lambda > 420$ nm.

DFT calculations with the periodic boundary conditions were carried out using a plane wave (PW) based program, Castep [52,53]. The Perdew-Burke-Ernzerhof (PBE) functional [54,55] was used together with the ultrasoft-core potentials [56]. The basis set cutoff energy was set to 300 eV. The electron configurations of the atoms were H: $1s^1$, O: $2s^2 2p^4$, S: $3s^2 3p^4$, and Ti: $3s^2 3p^6 3d^2 4s^2$. The lattice parameters were $a = 7.552 \text{ \AA}$, $b = 10.210 \text{ \AA}$, $\alpha = 88.99^\circ$, $\beta = \gamma = 90^\circ$. The surface normal was taken in the direction c, and $c = 30 \text{ \AA}$ including the vacuum region. The catalyst was modeled by a $(\text{TiO}_2)_{16}$ slab representing the (101) face of anatase structure. A single S atom as an impurity replaced Ti atom. For the hydrated surface, four water



Scheme 1. Schematic illustration of preparation of mesoporous $\text{Fe}_3\text{O}_4/\text{TiO}_2\text{-S}$ photocatalyst.

molecules were dissociated into OH and H, and they were bonded to Ti and O atoms on the surface, respectively.

2.3. Photocatalysis experiments

Photocatalytic studies were carried out in a photochemical reactor (Nanjing Xujiang, Ltd), which was equipped with a cold quartz tube and an inner Xenon lamp (350 W). A circulating water system was used to keep the reaction system at room temperature ($25 \pm 2^\circ\text{C}$), and an optical filter (Shanghai Seagull Colored Optical Glass Co., Ltd) was adopted to provide visible light ($\lambda > 420\text{ nm}$). Simulated solar light from the Xe lamp (350 W) was also provided to initiate the photoreaction without optical filter. Photocatalytic decomposition of RhB ($10\text{ }\mu\text{M}$) and formaldehyde ($50\text{ }\mu\text{M}$) aqueous solution was carried out with 20 mg of the powdered catalyst suspended in a Pyrex test tube (55 mL) with or without the addition of NaCl. UV-vis spectrometer (Hitachi U-3010) and GC-TCD were respectively employed to determine the degradation efficiency of dyes and formaldehyde molecules at given time intervals.

3. Results and discussions

The detailed procedure for preparing mesoporous $\text{TiO}_2\text{-S}$ coupled Fe_3O_4 photocatalysts is shown in the Experimental section. In brief, $\text{TiO}_2\text{-S}$ is prepared by a modified sol-gel method, which uses titanium sulfate as the dual template for TiO_2 and S, CTAB as a surface surfactant, and P123 as the template for mesostructure formation. Water-dispersible Fe_3O_4 nanoparticles are synthesized via a one-step reverse precipitation method in the presence of sodium citrate and ferrous sulfate. The coupling of Fe_3O_4 nanoparticles and $\text{TiO}_2\text{-S}$ to ultimately form $\text{Fe}_3\text{O}_4/\text{TiO}_2\text{-S}$ photocatalyst is accomplished by a hydrothermal treatment process. The whole procedure is schematically illustrated in Scheme 1.

Fig. 1a shows the XRD patterns and indexing of $\text{Fe}_3\text{O}_4/\text{TiO}_2\text{-S}$ samples with two magnetite loading amounts (3.5 and 6.7 wt%; hereafter denoted as 3.5- $\text{Fe}_3\text{O}_4/\text{TiO}_2\text{-S}$ and 6.7- $\text{Fe}_3\text{O}_4/\text{TiO}_2\text{-S}$, respectively), revealing that both of TiO_2 and Fe_3O_4 have good crystallization. No monophasic S is detected based on the XRD analysis, suggesting its successful doping into the TiO_2 crystals as S cations. TiO_2 and Fe_3O_4 species correspond to nanosized anatase (JCPDS, No. 211272) and magnetite crystals (JCPDS, No. 190629), respectively, which are consistent with the following

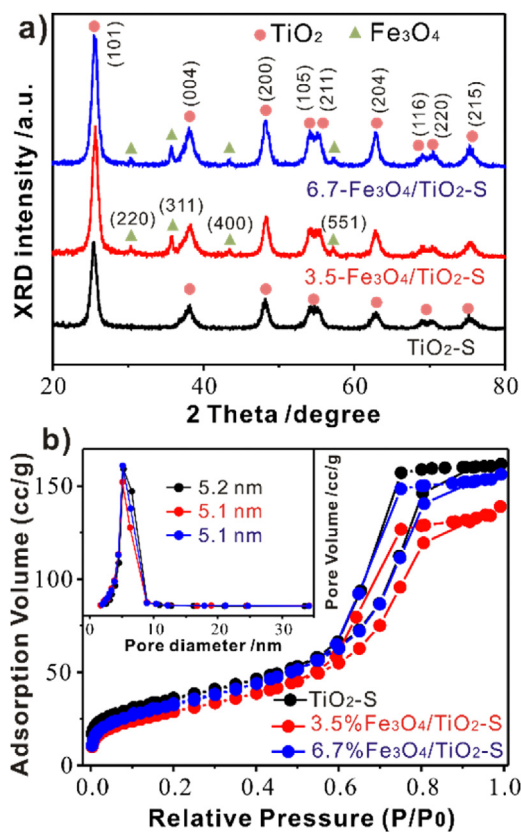


Fig. 1. (a) XRD spectra and (b) N_2 adsorption and desorption isotherms of $\text{TiO}_2\text{-S}$, 3.5- $\text{Fe}_3\text{O}_4/\text{TiO}_2\text{-S}$ and 6.7- $\text{Fe}_3\text{O}_4/\text{TiO}_2\text{-S}$ photocatalysts with their pore-size distributions (inset).

HRTEM analysis. As no diffraction peaks of rutile phase are observed in the spectrum, it is concluded that the as-prepared $\text{TiO}_2\text{-S}$ catalyst is in a pure anatase structure. The average crystalline size of anatase TiO_2 calculated from the broadening of the (101) XRD peak of anatase phase is 10.7 nm. Fig. 1b displays the nitrogen adsorption-desorption isotherms and the pore size distributions (inset) of $\text{Fe}_3\text{O}_4/\text{TiO}_2\text{-S}$ with different magnetite loadings. All of the isotherms are type IV with a H1 hysteresis loop, which is char-

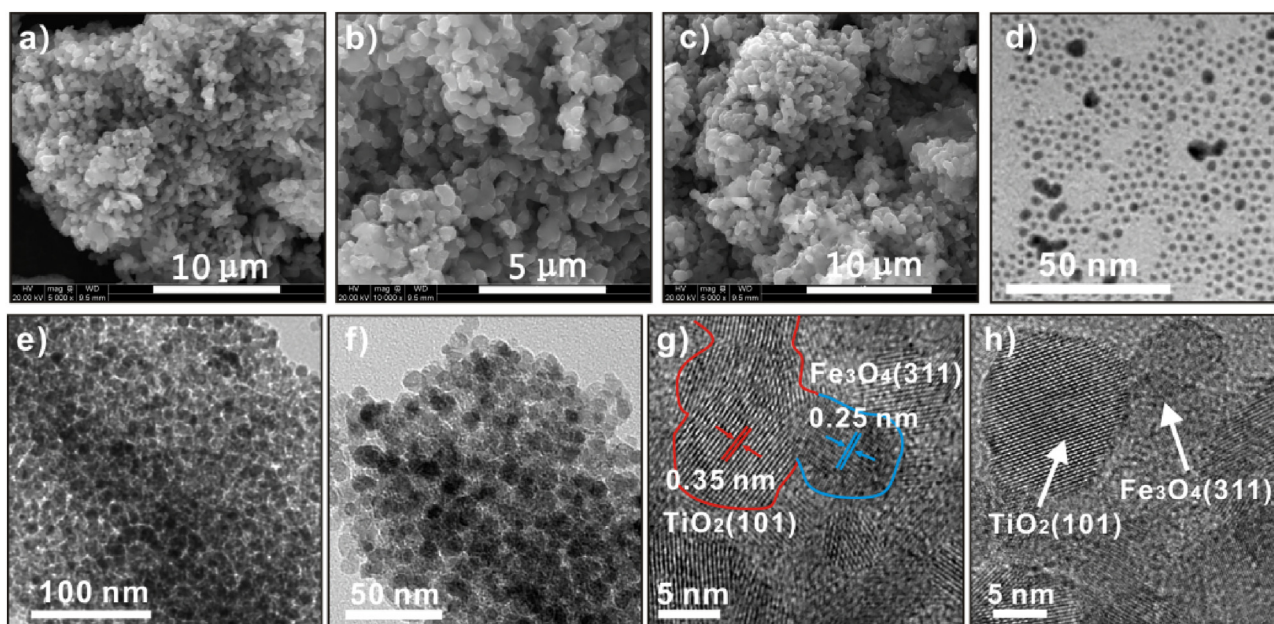


Fig. 2. SEM images of (a) $\text{TiO}_2\text{-S}$, (b) $3.5\text{-Fe}_3\text{O}_4/\text{TiO}_2\text{-S}$ and (c) $6.7\text{-Fe}_3\text{O}_4/\text{TiO}_2\text{-S}$; TEM images of (d) monodispersed Fe_3O_4 nanoparticles, (e) $3.5\text{-Fe}_3\text{O}_4/\text{TiO}_2\text{-S}$ and (f) $6.7\text{-Fe}_3\text{O}_4/\text{TiO}_2\text{-S}$, and HR-TEM images of (g) $3.5\text{-Fe}_3\text{O}_4/\text{TiO}_2\text{-S}$ and (h) $6.7\text{-Fe}_3\text{O}_4/\text{TiO}_2\text{-S}$.

Table 1

Physicochemical properties of $\text{TiO}_2\text{-S}$, $3.5\text{-Fe}_3\text{O}_4/\text{TiO}_2\text{-S}$ and $6.7\text{-Fe}_3\text{O}_4/\text{TiO}_2\text{-S}$ photocatalysts.

Sample	S_{BET} (m^2/g)	Pore volume (cm^3/g)	Pore diameter (nm)
$\text{TiO}_2\text{-S}$	126.5	0.19	5.2
$3.5\text{-Fe}_3\text{O}_4/\text{TiO}_2\text{-S}$	103.6	0.21	5.1
$6.7\text{-Fe}_3\text{O}_4/\text{TiO}_2\text{-S}$	116.7	0.24	5.1

acteristic of mesoporous materials. The pore size distribution of the sample is relatively narrow, and the average size is determined to be ~ 5.1 nm. Other physicochemical properties, such as surface area, pore volume and pore diameter of $\text{TiO}_2\text{-S}$, $3.5\text{-Fe}_3\text{O}_4/\text{TiO}_2\text{-S}$ and $6.7\text{-Fe}_3\text{O}_4/\text{TiO}_2\text{-S}$ photocatalysts are listed in Table 1, and no big difference is found for these materials.

The morphology of the as-synthesized $\text{TiO}_2\text{-S}$, $3.5\text{-Fe}_3\text{O}_4/\text{TiO}_2\text{-S}$ and $6.7\text{-Fe}_3\text{O}_4/\text{TiO}_2\text{-S}$ nanoparticles was analyzed by scanning electron microscope (SEM) and transmission electron microscope (TEM). Fig. 2a–c show the SEM images of $\text{TiO}_2\text{-S}$, $3.5\text{-Fe}_3\text{O}_4/\text{TiO}_2\text{-S}$ and $6.7\text{-Fe}_3\text{O}_4/\text{TiO}_2\text{-S}$ photocatalysts, respectively. It is seen that all of them have nice particle dispersity and smooth surfaces with the average size *ca.* 11.2 nm. In addition, TEM image of the as-synthesized Fe_3O_4 nanoparticles was shown in Fig. 2d, representing monodispersed character with average size *ca.* 3.5 nm. TEM observation also indicates that $3.5\text{-Fe}_3\text{O}_4/\text{TiO}_2\text{-S}$ and $6.7\text{-Fe}_3\text{O}_4/\text{TiO}_2\text{-S}$ samples possess wormhole-like mesostructures with short-range order only (Fig. 2e–f). The nanoparticles are less regular in diameter and randomly packing in a three-dimensional manner. It means that no ordered mesostructures are formed during catalysts preparation, but they can provide high surface area and enough mesopores for anchoring Fe_3O_4 nanoparticles as well as for fast mass transportation of the reactants, which is advantageous for photocatalytic reactions. The high-resolution TEM (HRTEM) images (Fig. 2g–h) clearly show the crystal lattice of anatase $\text{TiO}_2\text{-S}$ and Fe_3O_4 phases, as indicated by lattice fringes with interplanar spacing of 0.35 and 0.25 nm, corresponding to (101) planes of anatase TiO_2 and (311) planes of Fe_3O_4 , respectively, irrespective of the loading amount of Fe_3O_4 nanoparticles. It also demonstrates the successful formation of heterostructures between $\text{TiO}_2\text{-S}$ and Fe_3O_4 nanoparticles.

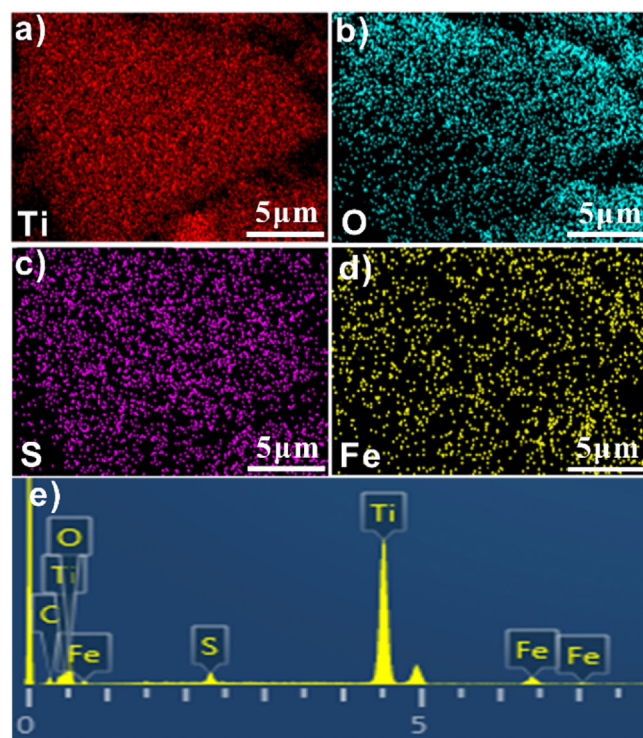


Fig. 3. EDS mapping of individual elements in $3.5\text{-Fe}_3\text{O}_4/\text{TiO}_2\text{-S}$: (a) Ti, (b) O, (c) S, (d) Fe, and (e) EDS spectrum of $3.5\text{-Fe}_3\text{O}_4/\text{TiO}_2\text{-S}$.

The excellent doping of S elements into TiO_2 nanocrystals as well as the high dispersion of Fe_3O_4 nanocrystals on TiO_2 surface are further verified by energy dispersive spectrometer (EDS) mapping (Fig. 3a–d) coupled with detailed element survey studies (Fig. 3e). EDS analysis reveals the co-presence of Ti, O, S and Fe elements in a typical $3.5\text{-Fe}_3\text{O}_4/\text{TiO}_2\text{-S}$ sample, indicating the homogeneous doping of S in TiO_2 crystallites.

Magnetic characterization using a magnetometer at 300 K indicates that the $3.5\text{-Fe}_3\text{O}_4/\text{TiO}_2\text{-S}$ and $6.7\text{-Fe}_3\text{O}_4/\text{TiO}_2\text{-S}$ samples have

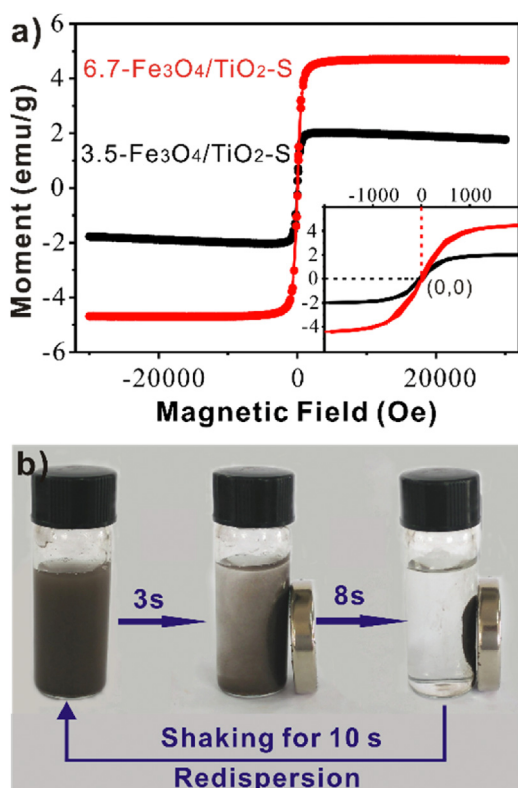


Fig. 4. (a) M-H curves of 3.5-Fe₃O₄/TiO₂-S and 6.7-Fe₃O₄/TiO₂-S recorded at room temperature, and (b) magnetic separation photographs of 3.5-Fe₃O₄/TiO₂-S in water.

magnetization saturation values of 4.7 and 2.1 emu/g (Fig. 4a), respectively. Additionally, no remanence is detected for both of the samples. The magnified hysteresis loops further confirm that the catalysts are superparamagnetic (inset, Fig. 4a). As a consequence, the nanoparticles in their homogeneous dispersion show prompt response to the applied magnetic field (1000 Oe) and re-disperse quickly with a slight shake once the magnetic field is retracted (Fig. 4b). It suggests that the nanoparticles possess excellent magnetic responsivity and redispersibility, which is an advantage to their succeeding photocatalytic applications.

The UV–vis diffuse reflectance spectra were utilized to analyze the optical properties and the band gap energy of the samples. In contrast to P25 TiO₂ that is only responsive to UV light, TiO₂-S exhibits a detectable absorption shoulder in the visible region (400–600 nm). In addition, Fe₃O₄/TiO₂-S samples show even much stronger visible light absorption band (Fig. 5a). The enhanced visible light response of Fe₃O₄/TiO₂-S is partially attributed to the synergetic effect of S-doping and surface hydroxyls, rather than the doping of Fe anions into the lattice of TiO₂, because the disorder structure of Fe-TiO₂ will lead to the local destruction of superparamagnetism, which is not observed in the aforementioned magnetic characterizations. In addition, based on the following equation: $(Ah\nu)^2 = h\nu - E_g$, which is valid for direct-band-gap materials, the band gap energies of TiO₂-S and 3.5-Fe₃O₄/TiO₂-S are estimated to be 2.89 and 2.81 eV, respectively (Fig. 5b). It means that these photocatalysts can be fully excited by visible light with wavelength shorter than 429 nm.

Rhodamine B (RhB) is often used as a tracer dye within water to determine the rate and direction of flow and transport, because its fluorescence can be detected easily and inexpensively with normal fluorimeters. However, RhB is suspected to be carcinogenic, and its complete decomposition is important to water purification. In addition, in common dyeing process, various mordants such as NaCl are included to enhance the color fastness of fabrics.

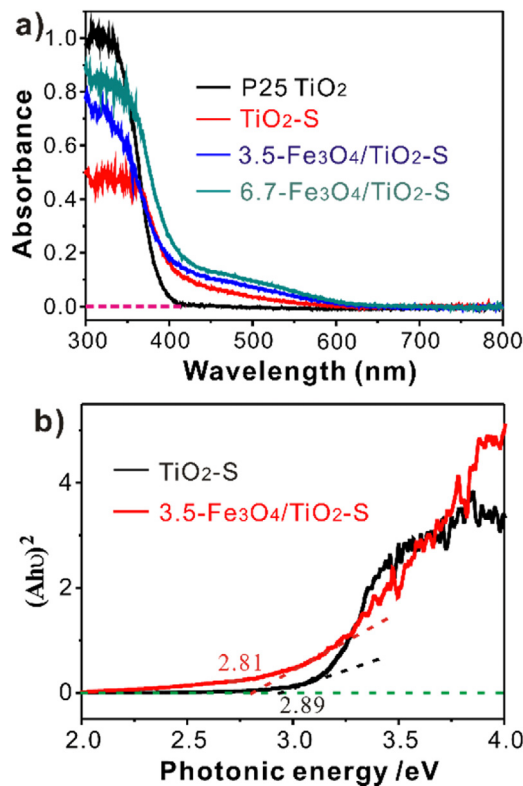


Fig. 5. (a) UV–vis spectra of P25 TiO₂, TiO₂-S, 3.5-Fe₃O₄/TiO₂-S and 6.7-Fe₃O₄/TiO₂-S photocatalysts and (b) their corresponding estimated band gaps.

Thus, dye waste solution usually contains tremendous mordants, which are often poisonous species to catalytic materials. Accordingly, herein, RhB solutions (10 μ M) with or without the addition of NaCl were employed to study the degradation efficiency of TiO₂-S based photocatalysts under visible light irradiation ($\lambda > 420$ nm). As shown in Fig. 6a, only negligible degradation of RhB pollutants was observed in a catalyst-free reaction system after 90 min of visible light irradiation, while almost all of NaCl-free RhB molecules were decomposed after 180 min when TiO₂-S was used. Interestingly, the photocatalytic activity of TiO₂-S was further improved by coupling with Fe₃O₄ nanoparticles: RhB dyes were completely degraded after 120 and 60 min when 6.7-Fe₃O₄/TiO₂-S and 3.5-Fe₃O₄/TiO₂-S were employed as the catalysts, respectively. By using 3.5-Fe₃O₄/TiO₂-S as the photocatalyst, the photographs of each RhB solution extracted in different time intervals clearly show the color evolution from purple to completely transparent (Fig. 6b). As for the NaCl-involving RhB solution (Fig. 6c), all of dye molecules were degraded with nearly 120 min visible light illumination over 3.5-Fe₃O₄/TiO₂-S photocatalyst, while 6.7-Fe₃O₄/TiO₂-S and TiO₂-S photocatalysts exhibited similar catalytic efficiency, which required more than 210 min to degrade the pollutants completely. In this case, the rate constants of the catalytic degradation of RhB over 6.7-Fe₃O₄/TiO₂-S and 3.5-Fe₃O₄/TiO₂-S were estimated to be 0.0341 and 0.0123 min⁻¹, respectively, as shown in Fig. 6d. It indicates that the degradation efficiency is enhanced by more than 2 times when proper amounts of Fe₃O₄ nanocrystals are coupled with TiO₂-S, and notably Fe₃O₄/TiO₂-S could smoothly play their photocatalytic functions even in the presence of high concentration of NaCl.

In a real environment, solar light is the most renewable and economical energy source for the application of photocatalysts. We thus further examined the photo-degradation of RhB pollutants under simulated solar light (350 W Xe lamp) irradiation over TiO₂-S based photocatalysts. Similar to visible light photocatalysis, there

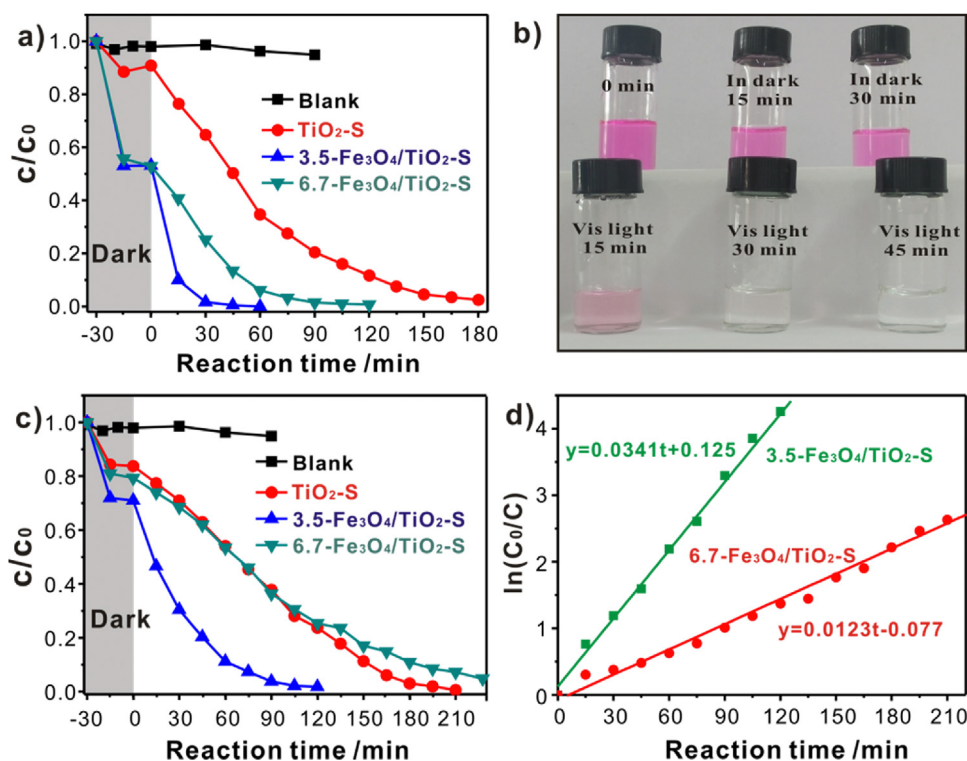


Fig. 6. (a) concentration changes of 50 mL NaCl-free RhB solution (10 μM) with or without $\text{TiO}_2\text{-S}$, $3.5\text{-Fe}_3\text{O}_4/\text{TiO}_2\text{-S}$ and $6.7\text{-Fe}_3\text{O}_4/\text{TiO}_2\text{-S}$ photocatalysts in the dark (30 min) and under visible light ($\lambda > 420\text{ nm}$), (b) photographs of each RhB solution extracted in different time intervals carried by $3.5\text{-Fe}_3\text{O}_4/\text{TiO}_2\text{-S}$ photocatalyst, (c) concentration changes of 50 mL RhB solution (10 μM) with 100 μM NaCl in the presence or absence of $\text{TiO}_2\text{-S}$, $3.5\text{-Fe}_3\text{O}_4/\text{TiO}_2\text{-S}$ and $6.7\text{-Fe}_3\text{O}_4/\text{TiO}_2\text{-S}$ photocatalysts in the dark (30 min) and under visible light ($\lambda > 420\text{ nm}$) and kinetic curves of $3.5\text{-Fe}_3\text{O}_4/\text{TiO}_2\text{-S}$ and $6.7\text{-Fe}_3\text{O}_4/\text{TiO}_2\text{-S}$ photocatalysts.

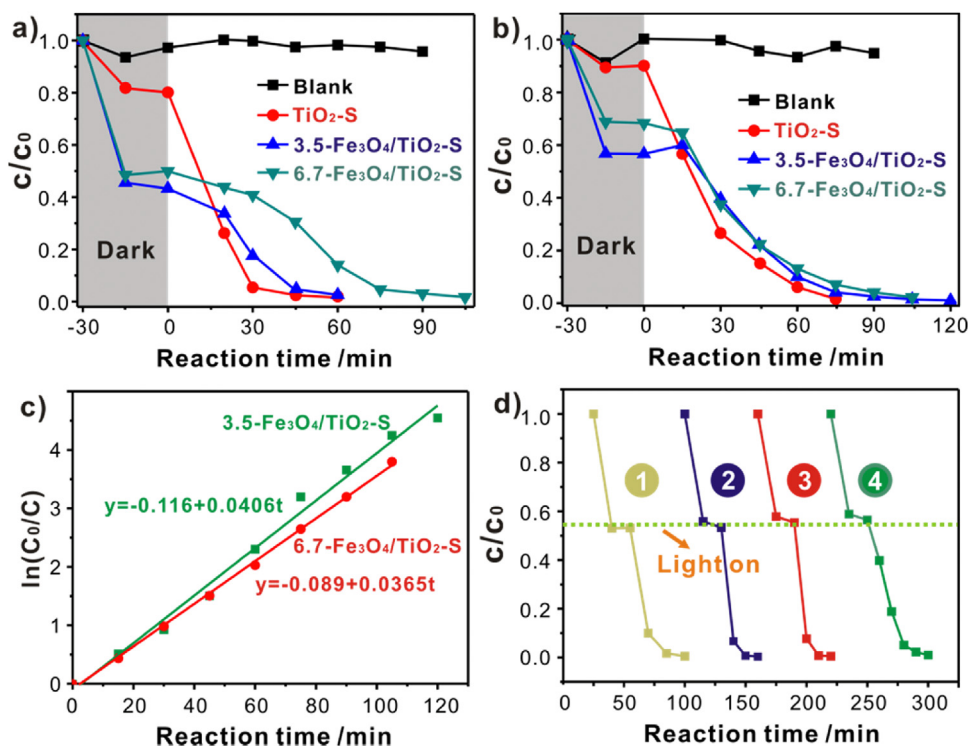


Fig. 7. Concentration changes of NaCl-free (a) and NaCl-involving (b) RhB solution with or without $\text{TiO}_2\text{-S}$, $3.5\text{-Fe}_3\text{O}_4/\text{TiO}_2\text{-S}$ and $6.7\text{-Fe}_3\text{O}_4/\text{TiO}_2\text{-S}$ photocatalysts in the dark (30 min) and under simulated solar light, (c) kinetic curves of $3.5\text{-Fe}_3\text{O}_4/\text{TiO}_2\text{-S}$ and $6.7\text{-Fe}_3\text{O}_4/\text{TiO}_2\text{-S}$ photocatalysts, and (d) repeated recycling experiments of $3.5\text{-Fe}_3\text{O}_4/\text{TiO}_2\text{-S}$.

was negligible degradation of NaCl-free RhB molecules under simulated solar light without catalysts. As shown in Fig. 7a, nearly 100%

molecules in 50 mL RhB solution were degraded in 60 min when $\text{TiO}_2\text{-S}$ was used. However, in contrast to the former visible light

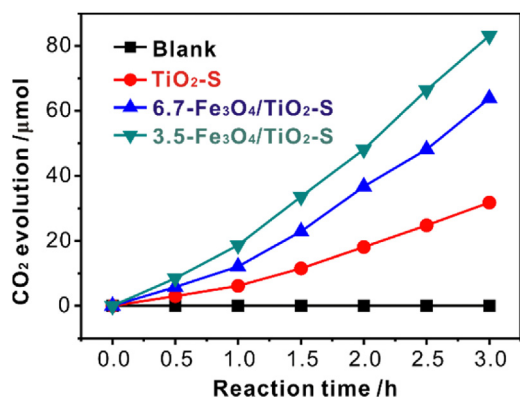


Fig. 8. Decomposition curves of formaldehyde solution over TiO₂-S, 3.5-Fe₃O₄/TiO₂-S and 6.7-Fe₃O₄/TiO₂-S photocatalysts under visible light ($\lambda > 420$ nm).

photocatalysis, when Fe₃O₄/TiO₂-S nanoparticles were used, its photocatalytic activity was even worse than that of TiO₂-S. This catalytic phenomenon was also observed by using NaCl-involving RhB solution as the substrate (Fig. 7b). As a result, kinetic studies showed that the degradation efficiency of RhB for 6.7-Fe₃O₄/TiO₂-S and 3.5-Fe₃O₄/TiO₂-S photocatalysts were in the same order of magnitude (Fig. 7c). This photocatalytic feature is reasonable because the simulated solar light contains a portion of UV light that can activate both of pristine TiO₂ and TiO₂-S, which reduces the effect of visible light photocatalysis. In addition to catalytic performance, stability is another important factor for practically useful catalysts, thus we examined the stability of 3.5-Fe₃O₄/TiO₂-S, which was demonstrated to be rather good with a 4-cycle experiment (Fig. 7d). Because iron leaching is always a serious problem for iron oxide-based catalysts during photocatalysis, we carried out ICP-MS to determine the residual iron concentration in the reaction mixture after photoreaction. The results showed that only negligible iron leaching occurred after photocatalytic reaction for 6 h in RhB solution. It may be partly attributed to the protection of Fe₃O₄ by mesoporous TiO₂ frameworks as well as their close contact. Furthermore, the SEM and TEM images of recycled 3.5-Fe₃O₄/TiO₂-S showed no obvious aggregation of Fe₃O₄ and TiO₂-S as compared with the fresh photocatalysts (Fig. S1 in the Supporting Information), demonstrating that Fe₃O₄/TiO₂-S could be used as a stable visible light photocatalyst for water purification purposes.

The most notable application of the present photocatalytic system is the photodecomposition of formaldehyde, which is a severe pollutant of both air and water as well as a general waste of many chemical industries [57]. Exposure to formaldehyde is detrimental to human health considering its widespread use, toxicity and volatility, thus its emission elimination has significant practical interest. The photocatalytic activity of TiO₂-S based photocatalysts was evaluated by oxidative decomposition of aqueous formaldehyde into gas-phase CO₂ under visible light irradiation ($\lambda > 420$ nm) and at room temperatures (ca. 25 °C). As shown in Fig. 8, formaldehyde alone was rather stable upon visible light irradiation, while it was readily decomposed into CO₂ over TiO₂-S. Surprisingly, the rate of CO₂ evolution was greatly enhanced by loading with Fe₃O₄ nanocrystals, and the photocatalytic efficiency of 3.5-Fe₃O₄/TiO₂-S (27.7 μmol h⁻¹) was ca. 2.6-fold and 1.3-fold higher than that of TiO₂-S (10.5 μmol h⁻¹) and 3.5-Fe₃O₄/TiO₂-S (21.2 μmol h⁻¹), respectively. The results further suggest that the integration of Fe₃O₄ nanocrystals is a promising strategy to promote the visible light photocatalytic performance of visible light responsive semiconductor.

In heterogeneous photocatalysis, reactive oxygen species is usually considered to be the main oxidant for organic decomposition. To address this, *in situ* EPR spectroscopy and spin-trapping tech-

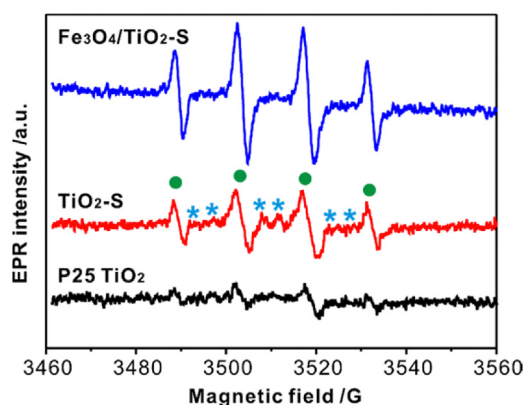


Fig. 9. *In situ* EPR spectra of DMPO adducts in aqueous methanol solution containing P25 TiO₂, TiO₂-S or 3.5-Fe₃O₄/TiO₂-S photocatalysts under visible light irradiation ($\lambda > 420$ nm).

nique were used as a semi-quantitative analysis to detect potential radicals that may be involved in the photocatalytic reactions. As shown in Fig. 9, when DMPO was used as the spin-trapping reagent and methanol as the sacrificial reagent, only distinguishable EPR signals appeared in the suspension containing P25 TiO₂ photocatalyst under visible light irradiation, while an obvious 1:2:2:1 quadruplet EPR peaks of DMPO-•OH adduct ($\alpha_N = \alpha_H = 14.05$ G; as indicated by solid circle) as well as a detectable sextet signal potentially corresponding to DMPO-•OOH adduct (indicated by stars) emerged in the photocatalytic system involving TiO₂-S. It implies that molecular oxygen may be reduced by surface trapped photoexcited electrons in accompany with surface hydroxyls to form hydrogenated peroxy species and subsequently underwent heterolytic dissociation into hydroxyl radicals. This chemical process may be significantly enhanced in the context of more hydroxyl groups on catalysts surface because the quadruplet DMPO-•OH adduct became much more remarkable when Fe₃O₄/TiO₂-S was used as the photocatalyst. It indicates that sufficient oxidants were produced during this photoreaction, which is consistent with the previous visible light initiated catalytic dye decomposition experiments as Fe₃O₄/TiO₂-S exhibited superior photoactivity than that of TiO₂-S. These experimental results also demonstrated that the narrowing band gap and the impurity levels in TiO₂ caused by S-doping and surface hydroxyl groups can stimulate the generation of photoexcited charge carriers and eventually lead to the production of oxidative hydroxyl radicals with visible light irradiation, which is a crucial catalytic step for organic decomposition. In addition, even though the determination of hydroxyl radical by EPR spin-trapping technique suggests that it may serve as the principal reactive oxidant for dye degradation using TiO₂-S based photocatalysts, it cannot exclude the possibility that photoexcited hole directly participates in the photocatalytic oxidation process as well, because in this EPR analysis methanol was used as sacrificial reagent for capturing holes.

Semiconductor photocatalysis is usually sensitive to the surface structures of photocatalysts, because some important factors, such as band gap can be easily tailored by surface engineering. Therefore, X-ray photoelectron spectroscopy (XPS) was employed to determine the surface properties of the photocatalysts. From the wide survey of XPS spectrum of TiO₂-S, only Ti, O, S, and C elements are observed (Fig. 10a). Specifically, the Ti 2p in TiO₂-S as well as 3.5-Fe₃O₄/TiO₂-S displays two peaks centered at 458.7 and 464.5 eV (Fig. 10b), which can be assigned to the binding energy of Ti 2p_{3/2} and Ti 2p_{1/2}, respectively. The presence of S is confirmed by a broad peak at ~168.5 eV, as shown in Fig. 10c. This peak can be further deconvoluted into separated peaks at 168.6 and 169.6 eV, which can be assigned to S 2p_{3/2} and S 2p_{1/2} respectively. Generally, the

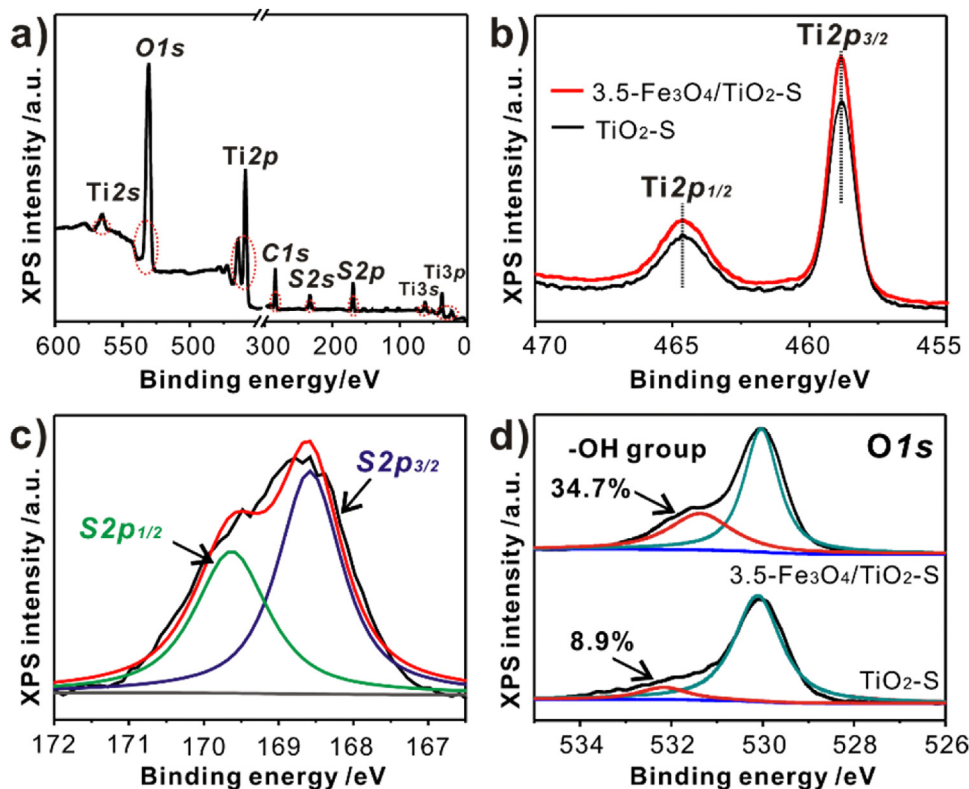


Fig. 10. XPS spectra of prepared TiO_2 and commercial P25 (a) Ti 2p and inset S 2p; (b) O 1s and the content of OH species.

peak at ~ 168.5 eV is ascribed to the S^{6+} states, with an appearance of S $2p_{3/2}$ peak about twice the intensity or area higher than that of S $2p_{1/2}$ peak. Hence, the S element could be S^{6+} species in the crystal lattice of TiO_2 -S, which is in agreement with previous studies [43]. It means that when Ti is substituted by S atom, SO_4 tetrahedral unit forms in the lattice. The O 1s XPS spectrum can be resolved into two peaks at ca. 529.9 and 531.7 eV (Fig. 10d), which are attributed to Ti–O crystalline oxygen and surface OH species, respectively. Interestingly, the percent of OH species in TiO_2 -S sample is only 8.9%, while it greatly increases to 34.7% in $3.5\text{-Fe}_3\text{O}_4/\text{TiO}_2$ -S. The enhancement of surface OH species can be ascribed to the hydrothermal treatment of TiO_2 -S to couple with Fe_3O_4 . The surface hydroxyl groups may positively affect the photocatalytic performance of TiO_2 -S in two main aspects: one is the introduction of surface hydrophilic property, which is advantageous to the adsorption of dyes in aqueous phase, and the other is the electronic interaction induced synergetic effect between S and hydroxyls. The latter effect is expected to result in the significant band gap narrowing, leading to the enhanced visible light photocatalytic activity of $\text{Fe}_3\text{O}_4/\text{TiO}_2$ -S, as discussed in detail later.

The band structures for normal TiO_2 (unit cell composition of $\text{Ti}_{16}\text{O}_{32}$), S-substituted TiO_2 (denoted as $\text{Ti}_{15}\text{O}_{32}\text{S}_1$), and S-substituted TiO_2 with surface hydroxyl groups (denoted as $\text{Ti}_{15}\text{O}_{32}\text{S}_1(\text{H}-\text{OH})_4$) were calculated using the Castep software. Fig. 11a–c shows the unit cells representing three models for the photocatalysts. In $\text{Ti}_{15}\text{O}_{32}\text{S}_1$ unit cell, a subsurface Ti atom of $\text{Ti}_{16}\text{O}_{32}$ is substituted by S atom (yellow atom in Fig. 11b). The OH groups on TiO_2 -S introduced by hydrothermal treatment actually mean that water is dissociated on TiO_2 surface. $\text{Ti}_{15}\text{O}_{32}\text{S}_1(\text{H}-\text{OH})_4$ unit cell indicates that four water molecules are dissociatively adsorbed, in which four H atoms are bonded to O atoms (Type I) and the rest of four OH groups are bonded to Ti atoms (Type II), as clearly revealed by dotted circles in Fig. 11c.

Figs. S2a–c in the Supporting Information show the band dispersion and the density of states (DOS) for the $\text{Ti}_{16}\text{O}_{32}$, $\text{Ti}_{15}\text{O}_{32}\text{S}_1$ and $\text{Ti}_{15}\text{O}_{32}\text{S}_1(\text{H}-\text{OH})_4$ unit cells, respectively. The DOS is divided into the angular momentum of atomic orbitals (AOs), represented by different line colors. In an effort to obtain more exact information on the atom-specific character of each band, the DOS is further decomposed into the AO-projected DOS (PDOS) in terms of atomic and angular momentum contributions. Fig. 12a and b show the AO-PDOS for O and Ti atoms, respectively, for the valence band and the lower part of conduction band of $\text{Ti}_{16}\text{O}_{32}$. The valence band is composed of O 2p orbitals (Fig. S3) and the conduction band consists of Ti 3d orbitals.

The conduction bands are shown in Fig. 12e and i for $\text{Ti}_{15}\text{O}_{32}\text{S}_1$ and $\text{Ti}_{15}\text{O}_{32}\text{S}_1(\text{H}-\text{OH})_4$ unit cells, respectively, and consist of the Ti 3d AO's, as well as pure TiO_2 . For $\text{Ti}_{15}\text{O}_{32}\text{S}_1$, the valence band is composed of the S 3sp and O 2p orbitals, as shown in Fig. 12c and d as well as Fig. S4. Importantly, the top of valence band is contributed by only the S atom, which essentially works to narrow the band gap of TiO_2 . This is explained in terms of the difference in electronegativity of S and O elements. It is interesting that both S 3s and 3p AO's contribute in a same degree (Fig. S5), since the energy difference between the S 3s and 3p AO's is small compared to that between the O 2s and 2p AO's.

For $\text{Ti}_{15}\text{O}_{32}\text{S}_1(\text{H}-\text{OH})_4$ unit cell (AO-PDOS for H, O, S and Ti atoms are shown in Fig. 12f–i), its occupied bands are composed of three parts. The lowest band in Figs. S6–S8 (~ 19 eV) is hybridization of the O 2s and H 1s AO's. Next lowest band is S 3s AO's (~ 10 eV). The third one is the valence band, and has a width of ~ 7 eV. The valence band is mainly composed of the O 2p and S 3p AO's, and the hybridization of the H 1s AO's occurs at the lowest part (~ 6 eV). Detailed analysis shows that there are no difference in the H 1s AO peaks derived from H–[O] and HO–[Ti]. At the top of valence band, the peak of O 2p AO's is depressed again and only the S 3p AO's contribute.

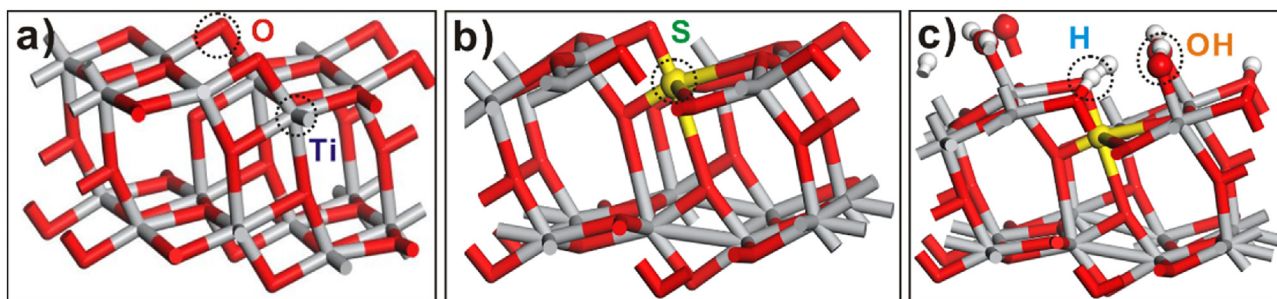


Fig. 11. Unit cell structures for (a) $\text{Ti}_{16}\text{O}_{32}$, (b) $\text{Ti}_{15}\text{O}_{32}\text{S}_1$ and (c) $\text{Ti}_{15}\text{O}_{32}\text{S}_1(\text{H}-\text{OH})_4$.

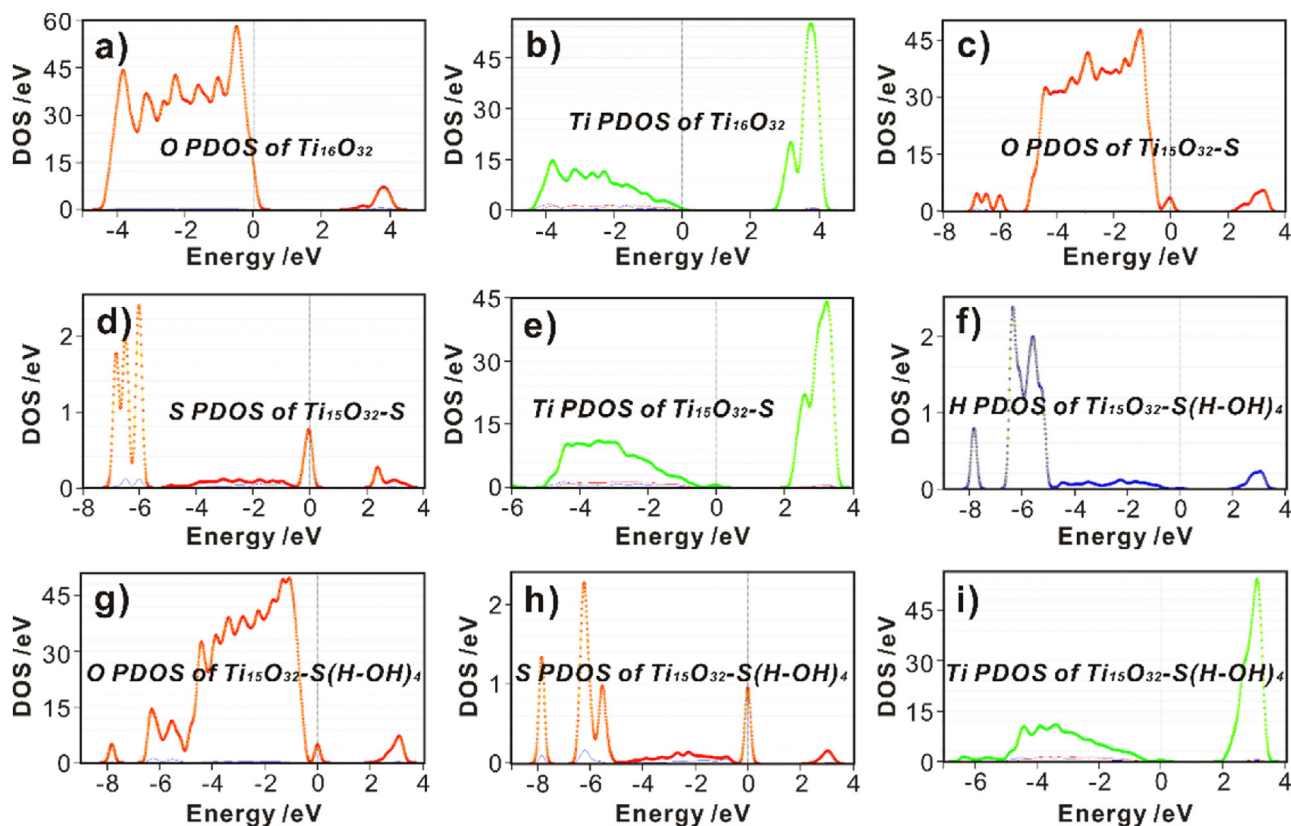


Fig. 12. Projected density of states (PDOS) for (a) O and (b) Ti of $\text{Ti}_{16}\text{O}_{32}$, (c) O, (d) S and (e) Ti of $\text{Ti}_{15}\text{O}_{32}\text{S}_1$, and (f) H, (g) O, (h) S, and (i) Ti of $\text{Ti}_{15}\text{O}_{32}\text{S}_1(\text{H}-\text{OH})_4$.

Unfortunately, in this kind of calculations, the energy of valence band maximum (VBM) is conveniently set to zero, and the absolute energies measured from vacuum are not known. To cope with this problem qualitatively, the peaks of O 2s AO's are lined up for the three systems, and the energies of VBM are compared each other. Even with rough estimate, the VBM's for $\text{Ti}_{15}\text{O}_{32}\text{S}_1$ and $\text{Ti}_{15}\text{O}_{32}\text{S}_1(\text{H}-\text{OH})_4$ are higher than that of $\text{Ti}_{16}\text{O}_{32}$ by 0.6 eV, and the top of the O 2p band rather than the VBM is almost the same among the three systems. Furthermore, the energy of the photogenerated holes in the valence bands is the highest in $\text{Ti}_{15}\text{O}_{32}\text{S}_1(\text{H}-\text{OH})_4$ among the three.

The density contour maps for the HOMOs (left part) and LUMOs (right part) of $\text{Ti}_{16}\text{O}_{32}$, $\text{Ti}_{15}\text{O}_{32}\text{S}_1$ and $\text{Ti}_{15}\text{O}_{32}\text{S}_1(\text{H}-\text{OH})_4$ are shown in Fig. 13a–c, respectively. The HOMO of $\text{Ti}_{16}\text{O}_{32}$ is composed of the O 2p AO's, whereas they are localized on the S 3p AO's for $\text{Ti}_{15}\text{O}_{32}\text{S}_1$ and $\text{Ti}_{15}\text{O}_{32}\text{S}_1(\text{H}-\text{OH})_4$. As for the LUMO, they are distributed on the Ti 3d AO's for the three systems. Adsorbed OH and H have no contribution to the frontier orbitals.

The band gaps are estimated to be 2.90, 2.47, and 2.19 eV, for $\text{Ti}_{16}\text{O}_{32}$, $\text{Ti}_{16}\text{O}_{31}\text{S}_1$, and $\text{Ti}_{15}\text{O}_{32}\text{S}_1(\text{H}-\text{OH})_4$, respectively. It decreases to 2.47 from 2.90 eV by the S atom substitution, and further decreases to 2.19 eV by the synergy effects of S atom and surface hydration, which is the smallest value among the examined photocatalysts. Although band gaps calculated by the present method are narrower than the actual ones, the order of the calculated band gaps is the same as that experimentally determined from diffuse reflectance spectra. The band gaps are also calculated for $\text{Ti}_{16}\text{O}_{32}(\text{H}-\text{OH})_4$ (dissociative adsorption of H_2O) and $\text{Ti}_{16}\text{O}_{32}(\text{H}_2\text{O})_4$ (molecular adsorption of H_2O) unit cells, and they are 2.74 and 2.79 eV, respectively (Figs. S9–S12 in the Supporting Information). These values are almost same as pure TiO_2 (2.90 eV). It means that individual surface hydroxyl modification or bulk S-doping alone has no such a great impact on band gap tailoring, but a synergetic effect emerges when they are coupled, which is able to largely decrease the forbidden band energy of TiO_2 .

The synchronous modification of surface and bulk state of TiO_2 by a dual nonmetal modification strategy is briefly illustrated in

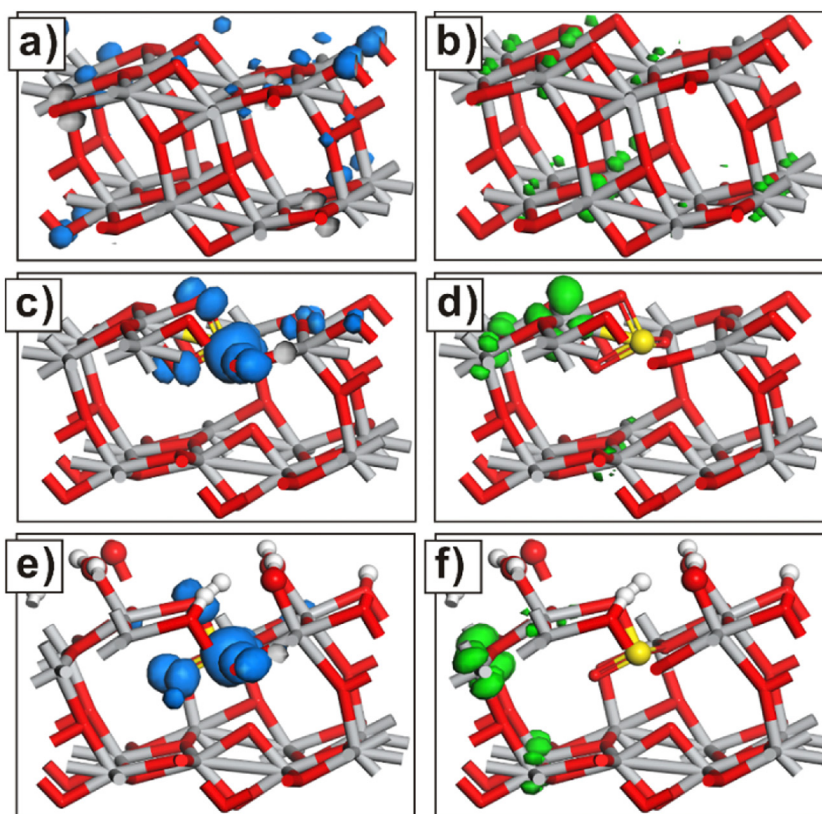
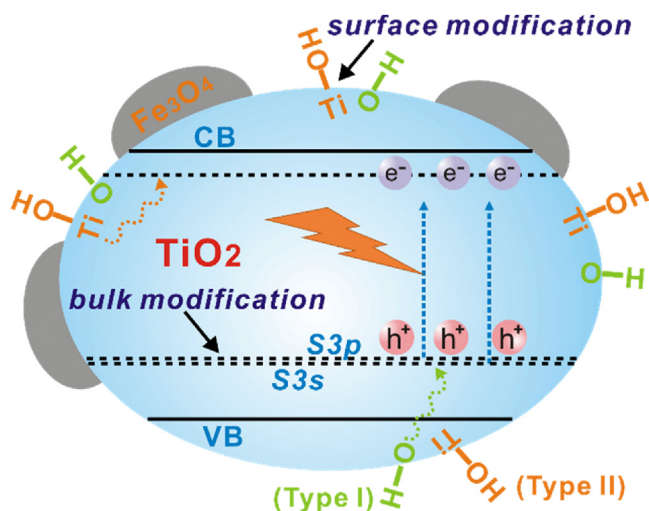


Fig. 13. Electron density contour maps of orbitals at the VBM (left part) and CBM (right part) regions for (a) $\text{Ti}_{16}\text{O}_{32}$, (b) $\text{Ti}_{15}\text{O}_{32}\text{S}_1$ and (c) $\text{Ti}_{15}\text{O}_{32}\text{S}_1(\text{H}-\text{OH})_4$.



Scheme 2. Schematic illustration of the synergistic effect of surface hydroxyls and S-doping in narrowing the band gap of TiO_2 , where Type I and Type II hydroxyls mean H atoms binding to O ($\text{H}-[\text{O}]$) and OH binding to Ti atoms ($\text{HO}-[\text{Ti}]$), respectively.

Scheme 2. This is the first case showing that electronic interactions between surface hydroxyls and the doped S are able to synergistically tailor the forbidden band energy of TiO_2 . In this case, we suggest that the band gap narrowing can be ascribed to the following reasons: (i) H atoms in Type I hydroxyls ($\text{H}-[\text{O}]$) can donate electrons to the bonding oxygen, and raise the VBM. On the other hand, HO groups in type II hydroxyls ($\text{HO}-[\text{Ti}]$) abstract electrons from neighboring Ti atoms, leading to downshift of CBM; (ii) As is reflected by Pauling electronegativity concept, S (2.5) is less electronegative than oxygen (3.5), which is beneficial to location of the S 3p AO's at higher energies than the O 2p AO's, contributing to

narrow the band gap; (iii) Formal valence band is thought to be constructed by the completion of octet on the O atoms, that is, O^{2-} anion. In pure TiO_2 , each Ti atom donates four electrons to O atoms. In the extreme expression of ionic compounds, it is represented as $\text{Ti}^{4+}(\text{O}^{2-})_2$. The S atom at the Ti site donates four electrons to O atoms. However, two electrons remain on the S atom, and these electrons generate a donor level at the above of the valence band of TiO_2 . This is also the reason that the HOMO is composed of S 3p AO's. As a result, the narrowing band gap and the impurity levels in TiO_2 caused by interplay of S-doping and surface hydroxyl groups can stimulate the generation of photoexcited charge carriers and eventually lead to the production of oxidative hydroxyl radicals in aqueous reaction environment with visible light irradiation, which is a decisive catalytic step for organic decomposition.

4. Conclusions

In summary, mesoporous S-doped TiO_2 photocatalyst coupled with superparamagnetic Fe_3O_4 nanoparticles was prepared by combining one-pot synthetic strategy and hydrothermal reaction using titanium sulfate as the dual precursor for both of TiO_2 and S. Interestingly, this synthetic strategy not only enabled the photocatalyst recyclable after photocatalysis, but also brought about a great portion of surface hydroxyls on TiO_2 . According to the theoretical calculations and experimental results, it is found that an electronic interaction induced synergistic effect of the surface hydroxyl groups and S atoms exists, which not only reduces the band gap of TiO_2 , making it responsive to visible light, but also introduces hydrophilicity for favorable adsorption of hydrophilic organic dyes and formaldehyde in aqueous solution. The synergistic effect finally leads to the production of oxidative hydroxyl radicals as the principle oxidant during photocatalysis. Therefore, the resulting photocatalyst exhibits promising photoactivity for

RhB and formaldehyde decomposition under both of visible light and solar light irradiation, and it also shows high tolerance on poisonous inorganic salts in photocatalytic systems. To our knowledge, this is the first example demonstrating that two different kinds of nonmetals synchronously modify the bulk and surface states of a typical semiconductor photocatalyst is beneficial to its band gap tailoring, which opens a new window to the future development of visible light photocatalyst in a low-cost and sustainable manner for practical applications.

Acknowledgements

We are grateful for financial support from the National Natural Science Foundation of China (No. 21503189 and 21403197) and Zhejiang Provincial Natural Science Foundation of China (No. LY15B030009).

Appendix A. Supplementary data

Supplementary data associated with this article can be found, in the online version, at <http://dx.doi.org/10.1016/j.apcatb.2017.06.022>.

References

- [1] R.P. Schwarzenbach, T. Egli, T.B. Hofstetter, U. von Gunten, B. Wehrli, Global water pollution and human health, *Annu. Rev. Environ. Resour.* 35 (2010) 109–136.
- [2] C. Wu, C. Maurer, Y. Wang, S. Xue, D.L. Davis, Water pollution and human health in China, *Environ. Health Perspect.* 107 (1999) 251.
- [3] R. Asahi, T. Morikawa, T. Ohwaki, K. Aoki, Y. Taga, Visible-light photocatalysis in nitrogen-doped titanium oxides, *Science* 293 (2001) 269–271.
- [4] J.-M. Herrmann, Heterogeneous photocatalysis: fundamentals and applications to the removal of various types of aqueous pollutants, *Catal. Today* 53 (1999) 115–129.
- [5] S. Malato, J. Blanco, A. Vidal, C. Richter, Photocatalysis with solar energy at a pilot-plant scale: an overview, *Appl. Catal. B-Environ.* 37 (2002) 1–15.
- [6] S. Malato, P. Fernández-Ibáñez, M.I. Maldonado, J. Blanco, W. Gernjak, Decontamination and disinfection of water by solar photocatalysis: recent overview and trends, *Catal. Today* 147 (2009) 1–59.
- [7] A. Mills, S. Le Hunte, An overview of semiconductor photocatalysis, *J. Photochem. Photobiol. A* 108 (1997) 1–35.
- [8] J. Peral, X. Domenech, D.F. Ollis, Heterogeneous photocatalysis for purification, decontamination and deodorization of air, *J. Chem. Tech. Biotech.* 70 (1997) 117–140.
- [9] M. Rauf, S.S. Ashraf, Fundamental principles and application of heterogeneous photocatalytic degradation of dyes in solution, *Chem. Eng. J.* 151 (2009) 10–18.
- [10] R. Li, W. Chen, H. Kobayashi, C. Ma, Platinum-nanoparticle-loaded bismuth oxide: an efficient plasmonic photocatalyst active under visible light, *Green Chem.* 12 (2010) 212–215.
- [11] X. Yan, X. Zhu, R. Li, W. Chen, Au/BiOCl heterojunction within mesoporous silica shell as stable plasmonic photocatalyst for efficient organic pollutants decomposition under visible light, *J. Hazard. Mater.* 303 (2016) 1–9.
- [12] A. Fujishima, T.N. Rao, D.A. Tryk, Titanium dioxide photocatalysis, *J. Photochem. Photobiol. C* 1 (2000) 1–21.
- [13] X. Chen, L. Liu, Y.Y. Peter, S.S. Mao, Increasing solar absorption for photocatalysis with black hydrogenated titanium dioxide nanocrystals, *Science* 331 (2011) 746–750.
- [14] S. Sakthivel, H. Kisch, Daylight photocatalysis by carbon-modified titanium dioxide, *Angew. Chem. Int. Ed.* 42 (2003) 4908–4911.
- [15] K. Nakata, A. Fujishima, TiO₂ photocatalysis: design and applications, *J. Photochem. Photobiol. C* 13 (2012) 169–189.
- [16] S.G. Kumar, L.G. Devi, Review on modified TiO₂ photocatalysis under UV/visible light: selected results and related mechanisms on interfacial charge carrier transfer dynamics, *J. Phys. Chem. A* 115 (2011) 13211–13241.
- [17] R. Li, H. Kobayashi, J. Guo, J. Fan, Visible-light-driven surface reconstruction of mesoporous TiO₂: toward visible-light absorption and enhanced photocatalytic activities, *Chem. Commun.* 47 (2011) 8584–8586.
- [18] R. Li, H. Kobayashi, J. Guo, J. Fan, Visible-light induced high-yielding benzyl alcohol-to-benzaldehyde transformation over mesoporous crystalline TiO₂: a self-adjustable photo-oxidation system with controllable hole-generation, *J. Phys. Chem. C* 115 (2011) 23408–23416.
- [19] R. Li, W. Chen, W. Wang, Magnetoswitchable controlled photocatalytic system using ferromagnetic FeO-doped titania nanorods photocatalysts with enhanced photoactivity, *Sep. Purif. Technol.* 66 (2009) 171–176.
- [20] M. Kapilashrami, Y. Zhang, Y.-S. Liu, A. Hagfeldt, J. Guo, Probing the optical property and electronic structure of TiO₂ nanomaterials for renewable energy applications, *Chem. Rev.* 114 (2014) 9662–9707.
- [21] D. Dvoranová, V. Brezová, M. Mazúr, M.A. Malati, Investigations of metal-doped titanium dioxide photocatalysts, *Appl. Catal. B-Environ.* 37 (2002) 91–105.
- [22] N. Serpone, Is the Band Gap of Pristine TiO₂ narrowed by Anion- and Cation-doping of Titanium Dioxide in Second-generation Photocatalysts? ACS Publications, 2006.
- [23] A.-W. Xu, Y. Gao, H.-Q. Liu, The preparation, characterization, and their photocatalytic activities of rare-earth-doped TiO₂ nanoparticles, *J. Catal.* 207 (2002) 151–157.
- [24] M.I. Litter, Heterogeneous photocatalysis: transition metal ions in photocatalytic systems, *Appl. Catal. B-Environ.* 23 (1999) 89–114.
- [25] S. Livraghi, M.C. Paganini, E. Giamello, A. Selloni, C. Di Valentin, G. Pacchioni, Origin of photoactivity of nitrogen-doped titanium dioxide under visible light, *J. Am. Chem. Soc.* 128 (2006) 15666–15671.
- [26] R. Asahi, T. Morikawa, H. Irie, T. Ohwaki, Nitrogen-doped titanium dioxide as visible-light-sensitive photocatalyst: designs, developments, and prospects, *Chem. Rev.* 114 (2014) 9824–9852.
- [27] M. Mrowetz, W. Balcerski, A. Colussi, M.R. Hoffmann, Oxidative power of nitrogen-doped TiO₂ photocatalysts under visible illumination, *J. Phys. Chem. B* 108 (2004) 17269–17273.
- [28] Y. Huang, W. Ho, S. Lee, L. Zhang, G. Li, J.C. Yu, Effect of carbon doping on the mesoporous structure of nanocrystalline titanium dioxide and its solar-light-driven photocatalytic degradation of NO_x, *Langmuir* 24 (2008) 3510–3516.
- [29] J.H. Park, S. Kim, A.J. Bard, Novel carbon-doped TiO₂ nanotube arrays with high aspect ratios for efficient solar water splitting, *Nano Lett.* 6 (2006) 24–28.
- [30] H. Liu, A. Imanishi, Y. Nakato, Mechanisms for photooxidation reactions of water and organic compounds on carbon-doped titanium dioxide, as studied by photocurrent measurements, *J. Phys. Chem. C* 111 (2007) 8603–8610.
- [31] W. Ren, Z. Ai, F. Jia, L. Zhang, X. Fan, Z. Zou, Low temperature preparation and visible light photocatalytic activity of mesoporous carbon-doped crystalline TiO₂, *Appl. Catal. B-Environ.* 69 (2007) 138–144.
- [32] L. Lin, W. Lin, J. Xie, Y. Zhu, B. Zhao, Y. Xie, Photocatalytic properties of phosphor-doped titania nanoparticles, *Appl. Catal. B-Environ.* 75 (2007) 52–58.
- [33] R. Zheng, L. Lin, J. Xie, Y. Zhu, Y. Xie, State of doped phosphorus and its influence on the physicochemical and photocatalytic properties of P-doped titania, *J. Phys. Chem. C* 112 (2008) 15502–15509.
- [34] K. Yang, Y. Dai, B. Huang, Understanding photocatalytic activity of S- and P-doped TiO₂ under visible light from first-principles, *J. Phys. Chem. C* 111 (2007) 18985–18994.
- [35] S. In, A. Orlov, R. Berg, F. García, S. Pedrosa-Jimenez, M.S. Tikhov, D.S. Wright, R.M. Lambert, Effective visible light-activated B-doped and N-codoped TiO₂ photocatalysts, *J. Am. Chem. Soc.* 129 (2007) 13790–13791.
- [36] A. Zaleska, J.W. Sobczak, E. Grabowska, J. Hupka, Preparation and photocatalytic activity of boron-modified TiO₂ under UV and visible light, *Appl. Catal. B-Environ.* 78 (2008) 92–100.
- [37] S. Liu, X. Chen, A visible light response TiO₂ photocatalyst realized by cationic S-doping and its application for phenol degradation, *J. Hazard. Mater.* 152 (2008) 48–55.
- [38] T. Umebayashi, T. Yamaki, H. Itoh, K. Asai, Band gap narrowing of titanium dioxide by sulfur doping, *Appl. Phys. Lett.* 81 (2002) 454–456.
- [39] J.C. Yu, W. Ho, J. Yu, H. Yip, P.K. Wong, J. Zhao, Efficient visible-light-induced photocatalytic disinfection on sulfur-doped nanocrystalline titania, *Environ. Sci. Tech.* 39 (2005) 1175–1179.
- [40] Y. Niu, M. Xing, B. Tian, J. Zhang, Improving the visible light photocatalytic activity of nano-sized titanium dioxide via the synergistic effects between sulfur doping and sulfation, *Appl. Catal. B-Environ.* 115 (2012) 253–260.
- [41] M. Zhou, J. Yu, Preparation and enhanced daylight-induced photocatalytic activity of C, NS-tridoped titanium dioxide powders, *J. Hazard. Mater.* 152 (2008) 1229–1236.
- [42] X. Chen, C. Burda, The electronic origin of the visible-light absorption properties of C-, N- and S-doped TiO₂ nanomaterials, *J. Am. Chem. Soc.* 130 (2008) 5018–5019.
- [43] M. Zhu, C. Zhai, L. Qiu, C. Lu, A.S. Paton, Y. Du, M.C. Goh, New method to synthesize S-doped TiO₂ with stable and highly efficient photocatalytic performance under indoor sunlight irradiation, *ACS Sustain. Chem. Eng.* 3 (2015) 3123–3129.
- [44] Y. Mizukoshi, N. Ohtsu, S. Semboshi, N. Masahashi, Visible light responses of sulfur-doped rutile titanium dioxide photocatalysts fabricated by anodic oxidation, *Appl. Catal. B-Environ.* 91 (2009) 152–156.
- [45] K. Kondo, N. Murakami, C. Ye, T. Tsubota, T. Ohno, Development of highly efficient sulfur-doped TiO₂ photocatalysts hybridized with graphitic carbon nitride, *Appl. Catal. B-Environ.* 142–143 (2013) 362–367.
- [46] C. Han, M. Pelaez, V. Likodimos, A.G. Kontos, P. Falaras, K. O'Shea, D.D. Dionysiou, Innovative visible light-activated sulfur doped TiO₂ films for water treatment, *Appl. Catal. B-Environ.* 107 (2011) 77–87.
- [47] Y.-H. Lin, H.-T. Hsueh, C.-W. Chang, H. Chu, The visible light-driven photodegradation of dimethyl sulfide on S-doped TiO₂: Characterization, kinetics, and reaction pathways, *Appl. Catal. B-Environ.* 199 (2016) 1–10.
- [48] P. Periyat, S.C. Pillai, D.E. McCormack, J. Colreavy, S.J. Hinder, *J. Phys. Chem. C* 112 (2008) 7644–7652.
- [49] B. Naik, K.M. Parida, C.S. Gopinath, *J. Phys. Chem. C* 114 (2010) 19473–19482.

- [50] S. Xuan, W. Jiang, X. Gong, Y. Hu, Z. Chen, J. Phys. Chem. C 113 (2008) 553–558.
- [51] T. Sugimoto, E. Matijević, J. Colloid Interface Sci. 74 (1980) 227–243.
- [52] M.C. Payne, M.P. Teter, D.C. Allan, T.A. Arias, J.D. Joannopoulos, Rev. Mod. Phys. 64 (1992) 1045–1097.
- [53] V. Milman, B. Winkler, J.A. White, C.J. Pickard, M.C. Payne, E.V. Akhmatkaya, R.H. Nobes, Int. J. Quantum Chem. 77 (2000) 895–910.
- [54] J.P. Perdew, K. Burke, M. Ernzerhof, Phys. Rev. Lett. 77 (1996) 3865–3868.
- [55] J.P. Perdew, K. Burke, M. Ernzerhof, Phys. Rev. Lett. 78 (1997) 1396.
- [56] D. Vanderbilt, Phys. Rev. B 41 (1990) 7892–7895.
- [57] Formaldehyde (gas) Report on Carcinogens, eleventh edition, U.S. Department of Health and Human Services, Public Health Service National Toxicology Program, 2005.